Hydrogeology Journal
https://doi.org/10.1007/s10040-024-02771-5

PAPER

Identification of the correlation between land subsidence and groundwater level in Cangzhou, North China Plain, based on time-series PS-InSAR and machine-learning approaches

Mouigni Baraka Nafouanti[1] · Junxia Li[1,2] · Hexue Li[3] · Mbega Ramadhani Ngata[4] · Danyang Sun[1] · Yihong Huang[1] · Chuanfu Zhou[1] · Lu Wang[1] · Edwin E. Nyakilla[5]

Received: 17 June 2023 / Accepted: 18 January 2024

Abstract

Land deformation is a severe environmental problem that is often caused by groundwater overexploitation. Traditional approaches, such as those based on ground leveling, are used as standard for monitoring land deformation, but they cannot collect enough information for land-deformation mapping. In this study, the time-series Persistent Scatterer Interferometry Synthetic Aperture Radar (PS-InSAR) was used as an improved method to identify land deformation in Cangzhou after the initiation of China's South-to-North Water Diversion Project (SNWDP). Machine learning (ML) models, including random forest and k-nearest neighbor, were used to determine the relationship between groundwater pressure and land deformation. The results showed that from 2018 to 2022, the deformation rate was up to –115 mm/year in Nanpi and Dongguang and varied between –57 and –26 mm/year in Qingxian and Cangxian. Land deformation after the SNWDP implementation was less than before. The ML models' results show that the accuracy of the random forest and k-nearest neighbor methods were 85 and 77%, respectively. Evaluation of the groundwater-level trend measured in six wells showed that after the SNWDP implementation, the groundwater pressure started to recover in Cangzhou, but a decline has been observed recently, particularly in 2022. The mean decrease in impurity (MDI) values demonstrates that aquifers IV and III contribute the most to land deformation in Cangzhou, with the highest MDI values of 33 and 26%, respectively. The study provides new insights into the evolution of regional land deformation, and the methods employed in this research can be adopted in other regions with similar conditions.

Keywords China · Groundwater level · Random forest · PS-InSAR · k-nearest neighbor

Introduction

Land subsidence is a relative sinking of the ground surface and is reported to be a common worldwide geohazard (L. Bai et al. 2022; X. Bai et al. 2022; Zhou et al. 2019). It has caused severe damage in numerous countries such as Pakistan, Nigeria, Italy, the United States, Australia, and Iran (Figueroa-Miranda et al. 2018; Guzy and Malinowska 2020; Holzer and Galloway 2005; Ng et al. 2015; Ohenhen and Shirzaei 2022; Ranjgar et al. 2021). In China, land deformation has been identified in several cities, such as Beijing, Tianjin, and Cangzhou in the North China Plain (NCP; Budhu and Adiyaman 2013). The rapid population and economic growth have intensified groundwater exploitation, leading to severe subsidence in the NCP (Shi et al. 2020; Ye et al. 2016). Cangzhou is one of the areas with a high population density, and groundwater is the primary water source

✉ Junxia Li
jxli@cug.edu.cn

1 School of Environmental Studies, China University of Geosciences, Wuhan 430074, China

2 MOE Key Laboratory of Groundwater Quality and Health, China University of Geosciences, Wuhan 430078, China

3 The Fourth Team of Hydrogeological and Engineering Geology, Hebei Bureau of Geo-Exploration, Hebei 061000, China

4 Laboratory of Theory and Technology of Petroleum Exploration and Development in Hubei Province, China University of Geosciences, Wuhan 430074, China

5 Department of Petroleum Engineering, Faculty of Earth Resources, China University of Geosciences, Wuhan 430074, China

Published online: 06 February 2024

for agricultural, industrial, and domestic purposes (L. Bai et al. 2022; X. Bai et al. 2022). Severe subsidence has been observed in the centre of Cangzhou since early 1972 (Guo et al. 2022). The most severe displacement in the centre of Cangzhou reached up to 2 m between 1972 and 2005 resulting from groundwater overexploitation (Zhou et al. 2018). Therefore, understanding human factors responsible for land deformation is necessary for better safety management.

Land subsidence has been reported to be a direct consequence of many natural and human factors (Argus et al. 2005; Pinel et al. 2011)—for instance, the overexploitation of groundwater constitutes the main anthropogenic activity triggering land subsidence (Arabameri et al. 2021b). In Cangzhou, studies demonstrated that the overextraction of groundwater, especially from the deep aquifer, has increased the subsidence in the area (L. Bai et al. 2022; X. Bai et al. 2022; Zhou et al. 2018). To control land subsidence and the overexploitation of groundwater, the government launched the South-to-North Water Diversion Project (SNWDP) in 2003, which involved drawing river water from the south to the north of China (Sun et al. 2022). The SNWDP transfers water from abundant regions to water scarcity areas, and the project has transferred about 49.4 billion m^3 of water to the NCP since its commission in 2014 (Wang et al. 2020). Furthermore, it has been suggested that land subsidence results from the interactions of multiple natural factors and processes such as lithology, geology, hydrodynamics, and land surface pressure (Abdollahi et al. 2019; Arabameri et al. 2021b). Studies have found that soil compression caused by water extraction undergoes rheologic deformation, and clayey soil, gravel, and sand aquifers may deform (Gong et al. 2018; Sivasithamparam et al. 2015). Cangzhou has silty and clay soils with relatively large flexibility, thus making it more likely to experience permanent subsidence (Guo et al. 2015); therefore, controlling and monitoring land subsidence using technology models is required.

Remote sensing (RS) technologies, including Interferometry Synthetic Aperture Radar (InSAR) and Differential Interferometry Synthetic Aperture Radar (D-InSAR), have demonstrated considerable ability to measure land subsidence (Feng et al. 2023; Pourkhosravani et al. 2022; Schlögel et al. 2015). Previous investigations have used D-InSAR to accurately identify ground displacement on a regional scale (Prati et al. 2010; Xu et al. 2016; Zhao et al. 2012). The method has been utilized frequently to monitor landslides (Yao et al. 2021), quantify surface subsidence (Raz et al. 2020), and monitor seismic activity (Govil et al. 2019) and deformation (Hussain et al. 2022a). However, D-InSAR is susceptible to environmental factors that have spatiotemporal distribution, such as atmospheric effects and temperature and humidity variations, which restricts its competence to measure long-term surface deformation with high accuracy. InSAR has demonstrated considerable ability in various disciplines to monitor and predict catastrophes (Khan et al. 2022; Rateb and Abotalib 2020). It has been employed to monitor landslides (Hussain et al. 2022b), subsidence (Arangio et al. 2014; Hilley et al. 2004), and displacement caused by earthquakes (Gahalaut 2009; Ruiz-Armenteros et al. 2018). InSAR techniques, such as persistent scatter interferometry synthetic aperture radar (PS-InSAR), have recently been employed to monitor land subsidence (Cigna and Tapete 2021; Yang et al. 2018). PS-InSAR is a new technique that can solve the difficulties faced using the D-InSAR process (Colesanti et al. 2003). This method has exclusive features for solving anomalies produced by backscattering and atmospheric delay to enhance the accuracy of deformation measurements (Borghero 2018). It has been employed widely in several areas—such as Beijing (Zuo et al. 2019), Spain (Mateos et al. 2017), African countries (Beladam et al. 2019; Cian et al. 2019), and Iran (Khorrami et al. 2020)—to quantify land deformation and yield satisfactory results. Also, machine learning (ML) models have been mainly employed for land subsidence studies (Arabameri et al. 2021b; Jordan and Mitchell 2015; Rahmati et al. 2019a, b). Random forest (RF) is an ML algorithm that can handle missing values and avoid overfitting problems in the dataset. It has been employed to predict land subsidence caused by groundwater extraction in Iran (Rahmati et al. 2019a, b). Likewise, the k-nearest neighbor (KNN) algorithm has more advantages because it is flexible, efficient to deploy in a complex dataset, and has been employed to solve diverse problems (Tovar-Gómez et al. 2013; Wang et al. 2015); therefore, in Cangzhou, several studies have used the PS-InSAR technique to identify subsidence in the area (L. Bai et al. 2022; X. Bai et al. 2022; Guo et al. 2015; Zhou et al. 2018; Zhu and Guo 2014). However, studies have focused on analyzing subsidence in previous years before the implementation of the SNWDP in Cangzhou; therefore, this study investigated the land subsidence after the SNWDP commenced operation. Additionally, ML models were employed to determine the relationship between groundwater and land deformation, which has not been explored in previous studies.

The main objective of this present research is to quantify the land deformation in Cangzhou from 2018 to 2022 with the advanced PS-InSAR technique. Second, RF and KNN were used to determine the relationship between groundwater and land deformation. This research provides new insight into understanding the current land deformation situation in Cangzhou. The improved ML techniques employed in this study to determine land subsidence and its relationship with groundwater can be applied in various areas worldwide.

Study Area

Cangzhou is located in the North China Plain in the coastal area of the Bohai Sea (Fig. 1). The site has flat land from southwest to northeast. Cangzhou is formed of different

plains, including the alluvial plain, the alluvial marina plain, and the marine plain in the west, centre, and eastern part, respectively (Wang et al. 2009). Land salinization and poor drainage affect the coastal zone of Cangzhou (Sun et al. 2022). Four aquifers in the Quaternary sediments underlie Cangzhou aquifer I, which is made of fine sand with a depth between 20 and 30 m. Aquifer II is formed of clay with medium sand ranging from 120 to 170 m depth (Zhou et al. 2018); however, the groundwater in these two aquifers is affected by seawater intrusion, which leads to high salinity. Aquifers III and IV are made of clay, gravel, and sand at depths from 250 to 380 m and 380 to 500 m, respectively (Li et al. 2014). Groundwater in deep confined aquifers III and IV is used as a primary water source for drinking and irrigation due to the good water quality. The shallow groundwater is replenished by surface-water infiltration, precipitation, and lateral flow, whereas the recharge to deep groundwater comes from lateral flow, compaction, and pore water from the clayey sediments (Zhang et al. 1997).

In recent decades, Cangzhou has experienced a water shortage caused by the high groundwater extraction rate. The water resources have been reduced by 60% due to the lack of precipitation and the drying-up of rivers, leading to droughts (Zhou et al. 2020). The increasing demand for water in the area has intensified the overexploitation of groundwater, which provides almost 80% of the total water supply (Zhou et al. 2019). The long-term groundwater abstraction led to the largest depression cones of the NCP, with a maximum head decrease of 100 m by 2005 (Gong et al. 2018), from which the significant groundwater decline triggered severe land subsidence of more than 2,000 mm. To solve the water shortage associated with confined aquifers, the government implemented a policy in 2005 to limit groundwater extraction; thus, surface water was transferred from the Dalangdian reservoir (Pang et al. 2014).

Methodology

Dataset Description

This research used Sentinel-1 C-band SAR images collected from January 2018 to December 2022 (ASF DAAC 2015); therefore, 62 SAR images were collected in ascending tracks and processed in SARPROZ software to identify the ground displacement in the study area. Sentinel-1 has

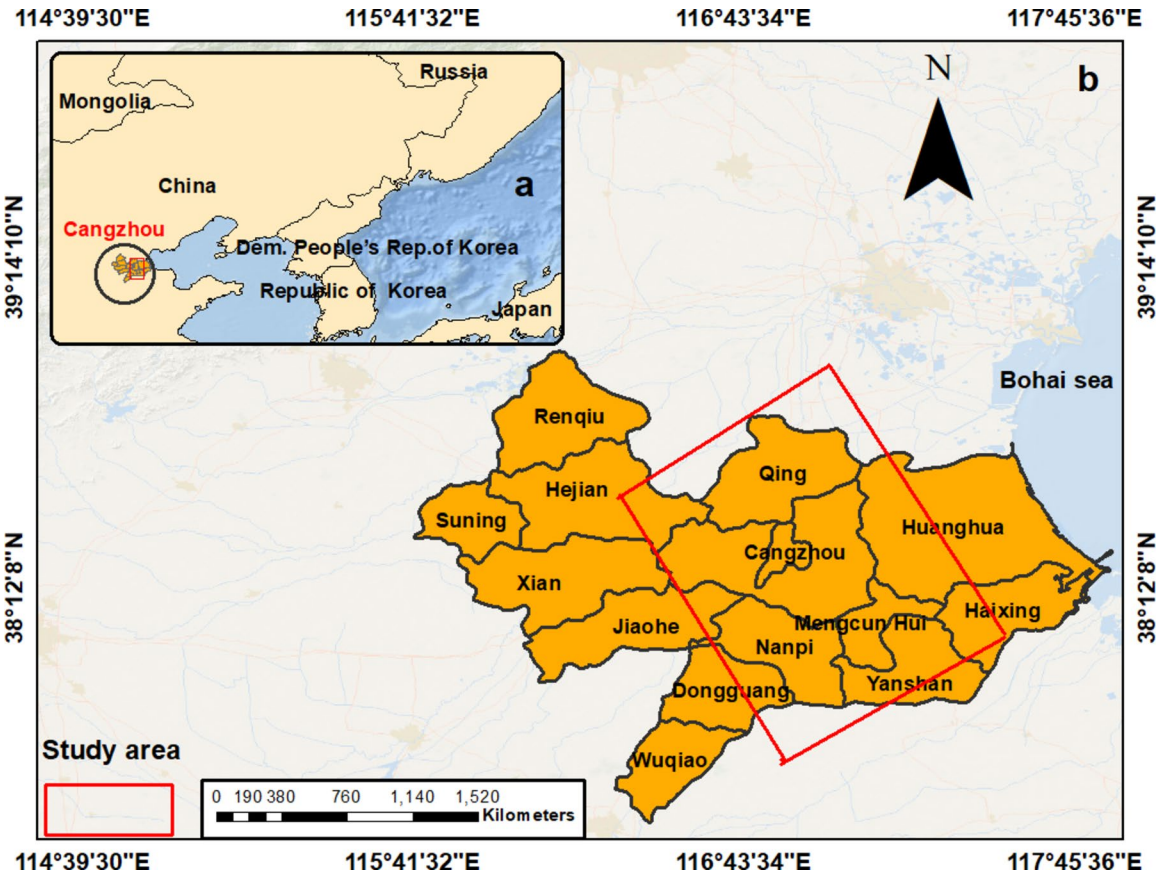

Fig. 1 **a** The location of the study area in China. **b** Map of the study area showing county boundaries

advantages due to its wide range, which covers 250 km in an interferometric wide swath mode and has an adequate resolution of 20 m in the azimuth and 5 m in the range direction (Hooper et al. 2012; Schmidt et al. 2015). Terrain observation by progressive scan (TOPS) mode divides the single scene into three sub-swaths that ensure the same image quality throughout the swath. Interferometric wide (IW) strip maps (SM), extra-wide swaths (EW), and waves (Wave) are acquisition modes for Sentinel-1 datasets (Da Lio et al. 2018; Schneider et al. 2006). The IW mode has been employed to collect the SAR images, which cover a single scene with an area of 250 km^2. The SAR images have significant spatial and temporal resolution with a short running time and are adequate to study subsidence scenarios from satellites (Kaneda et al. 2008). The description of the datasets employed in this study is presented in Table S1 in the electronic supplementary material (ESM), and a flowchart of the persistent scatter interferometry process is shown in Fig. 2.

Persistent scatter interferometry (PS-InSAR Technique)

Persistent scatter interferometry (PSI) is an approach proposed by Ferretti (Prati et al. 2010). The method can extract the target points with a stable radiometry property and identify surface deformation by separating the topographic phase of the ground targets (Dehghani et al. 2013; Zhao et al. 2009). In this work, the deformation of the study area was acquired using PS-InSAR in SARPROZ. The deformation phase can be achieved by employing the PSI process based on Eq. (1):

$$\Delta\varnothing_{int} = \varnothing_{flat} + \varnothing_{topo} + \varnothing_{def} + \varnothing_{atm} + \varnothing_{noise} \quad (1)$$

The interferometric stage is presented as $\Delta\varnothing_{int}$, $\varnothing_{flat}$ is the flat phase of the earth, and $\varnothing_{topo}$, which is the topographic phase, can be replaced by the digital elevation model (DEM) in SARPROZ. The deformation phase is known as $\varnothing_{def}$ which is the deformation in the line of sight (LOS), such as the vertical and horizontal movement. Also, $\varnothing_{atm}$ is the phase component of the atmospheric phase delay and $\varnothing_{noise}$ is the noise phase, including noise and other error components. The LOS can be converted into vertical movement by the following equation:

$$d_v = d_{LOS}/\cos\theta \quad (2)$$

where d_v represent the vertical movement, d_{LOS} is the line-of-sight displacement, and $\cos\theta$ represents the angle between the line-of-sight (LOS) and the vertical direction.

This technique detects coherent pixels over a time series analysis and requires more than 20 images to proceed (Vickers 2017). In this study, 62 images were employed, and a flowchart of the PSI workflow procedure in SARPROZ is shown in Fig. 2. The images used in this research had identical rotations with ascending orbits. The

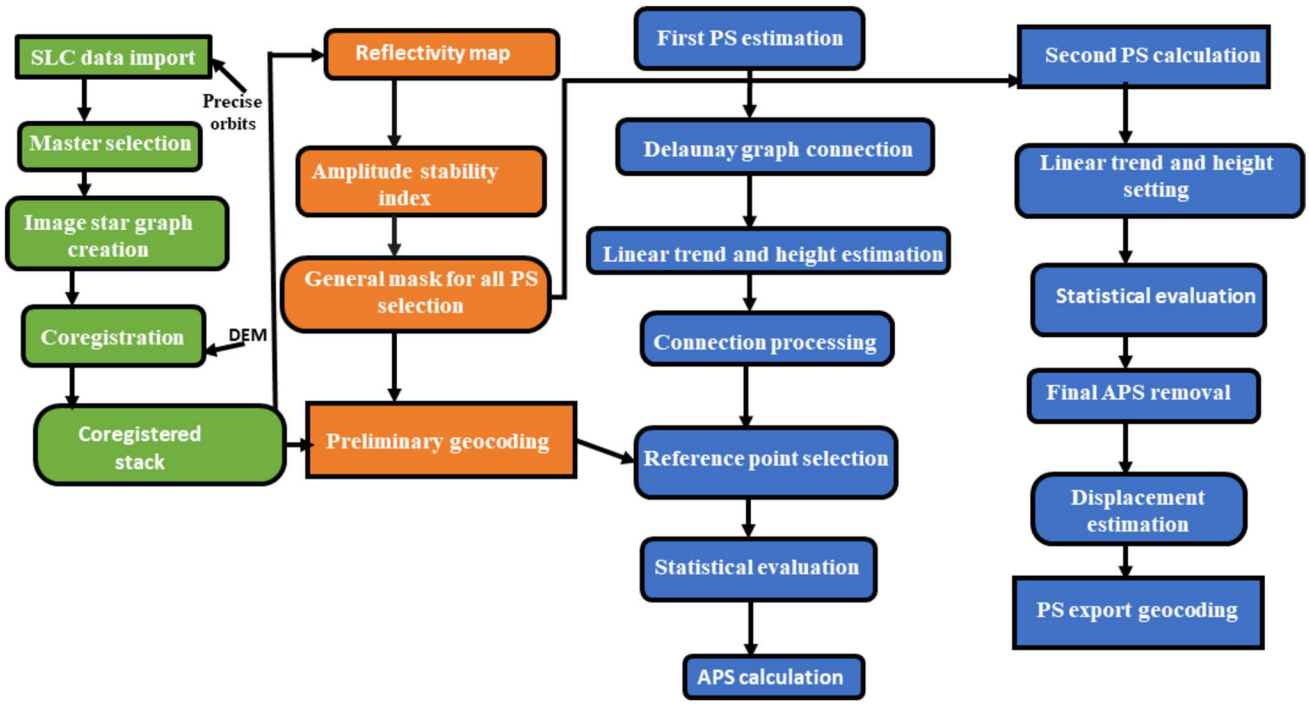

Fig. 2 The process of persistent scatter interferometry in SARPROZ

extraction of the master image was the first step based on the stack interferogram coherence using Eq. (3):

$$\gamma^k = \frac{1}{N}\sum_{i=1}^{N} g\left(B_{\lambda}^{s,k}, B_{\lambda.\max}\right) g\left(T^{s,k}, T_{\max}\right) g\left(f_{\mathrm{dc}}^{s,k}, f_{\mathrm{dc,max}}\right) \quad (3)$$

where γ^k is the cumulative coherence for master image k, and s is used as an index or identifier associated with k. $B_{\lambda.\max}$, $T_{\max}$, and $f_{\mathrm{dc,max}}$ are the maximum values for the perpendicular spatial baseline, temporal baseline, and Doppler centroid frequency, respectively. g represents the function used to process the parameters associated with spatial and temporal baselines. In the master extraction step, a temporal baseline distribution is formed between master and slave images (Fig. 3). The images were then categorized, and the specified area was selected and analyzed; furthermore, the topographic and flat terrain influences were removed by utilizing external DEM and orbital data. Persistent scatter (PS) candidates were chosen based on SAR analysis by calculating the amplitude stability index (ASI). The ASI Eq. (4) can be seen in the following:

$$\mathrm{ASI} = \frac{\sigma_a}{\eth} = \frac{\sqrt{\frac{\sum_{i=1}^{N}\left(|S_i| - |S|\right)^2}{N}}}{\frac{1}{N}\sum_{i=1}^{N}|S_i|} \quad (4)$$

N means the number of images, σ_a is the standard deviation, $\eth$ is the average value of the amplitude, S is the mean magnitude or amplitude of each value. Selecting an ASI threshold above 0.75 is recommended (Lei et al. 2016). In this work, the threshold for the ASI was 0.80 for the first PS selection; therefore, the Delaunay graph established a network by connecting the PS-selected points to create a triangular area that optimally covers the area of interest (Hussain et al. 2022a). This step calculates the differential residual topographic error and deformation velocities. Then, parameters were estimated using a linear model (linear displacement velocities and residual height), and the deduction of the atmospheric phase screen (APS) was assessed in the residual phases by graph inversion. The usual way to estimate the displacement is to use a linear model, which can be expressed as in the following equation:

$$\Delta\varphi_{s,k}^{\mathrm{disp}}(p) = \frac{4_{\mu}}{\gamma}\Delta_{\partial}(p)B_{t,s} \quad (5)$$

Δ_{∂} is the speed with target p, and $B_{t,s}$ is the temporal baseline, k and s are the parameters of combination for the selected reference point, and t represents the time. In this step, it is necessary to choose a stable reference point to fix the velocity values (a stable point is a chosen point on the ground).

The second phase of analysis was the second PS selection, and the ASI used was 0.69 to produce more concentrated PS points. The last step was APS removal using the same parameters and reference points for APS estimation.

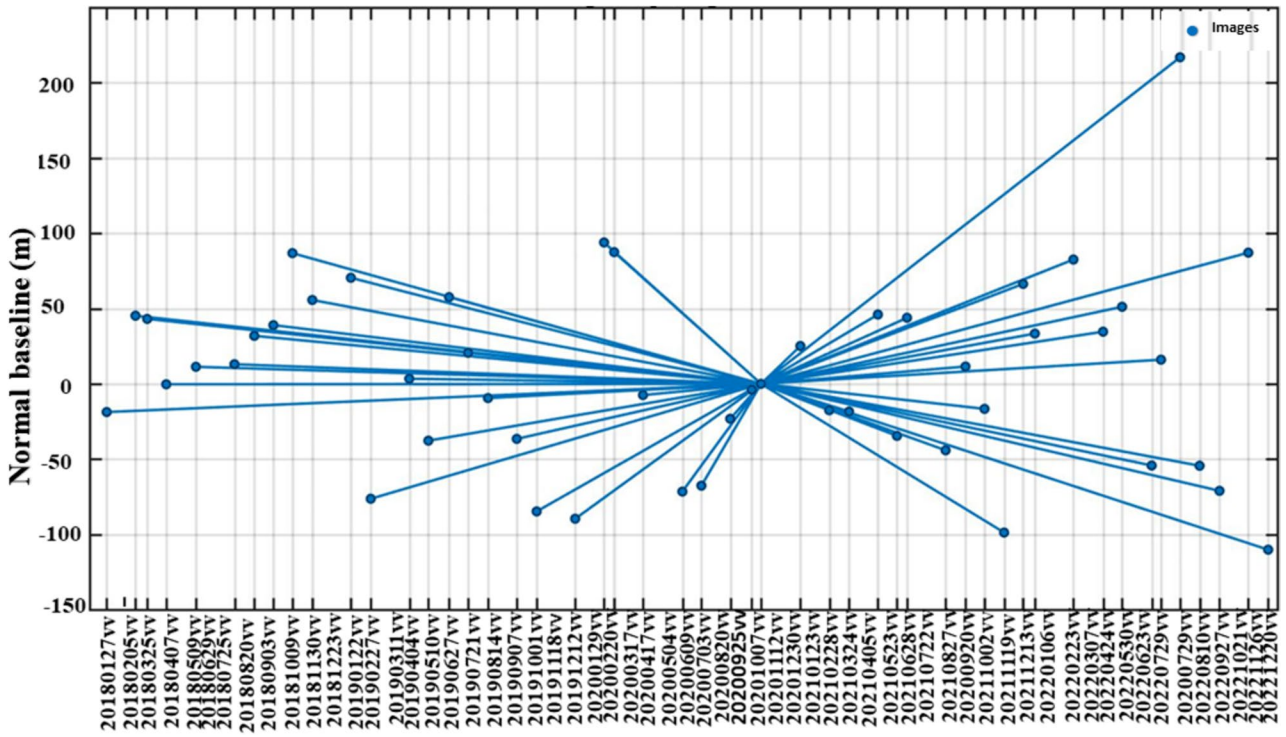

Fig. 3 The temporal baseline between master and slave images (shown as blue circles), collected from 2028 to 2022, in ascending tracks

In this step, the temporal coherence of PS was estimated to identify the APS veracity, generating satisfactory results higher than 0.7 (Fig. 4). Finally, PS was displayed using the scatter plot module and the geocoding in Google Earth and exported in ArcGIS.

Groundwater level variations

Groundwater level elevation was obtained from six wells in Aquifer IV to understand the confined aquifer's piezometric variations. Well measurements were obtained from fieldwork conducted between 2017 and 2022, and the data were obtained automatically using a water level probe. It is well recognized that piezometric levels vary seasonally due to weather changes and agricultural activity; therefore, the data for the six wells were acquired each November to observe the groundwater level trend. The locations of the six wells can be observed in Fig. 5a.

Modeling development and data preparation

In all, 250 groundwater level measurements were collected from 4 aquifers (I, II, III, and IV) in July 2022 and used to understand the relationship between groundwater and land subsidence. Therefore, the models include four inputs, including the groundwater level of aquifers I, II, III, and IV, with the land subsidence as output. The data were converted into low and high categories, and as a binary classification analysis, deformation rates above –3 mm/year are considered significant (Suksathien et al. 2022); thus, deformation more than –3 mm/year is classified as 1, and deformation less than –3 mm/year is classified as zero. Random forest (RF) and k-nearest neighbor (KNN) machine learning models were used in this study to predict the relationships between groundwater and land deformation in the study area. The RF approach utilizes numerous trees to form a robust and accurate model. For model development, randomness is introduced in two ways: first, there is a random selection with replacement of all data rows, which results in one-third of the data not being selected for a given tree (referred to as "out of bag" samples), and secondly, there is a restricted number of randomly selected variables made available at each node (Podgorski et al. 2018). The RF is defined as Eq. (6):

$$y = \frac{1}{n}\sum_{i}^{n} = p_i \tag{6}$$

where y is the label for an instance, n is the number of trees, and p_i signifies each tree's prediction. The model's dimension tree can be controlled by setting the necessary samples at the tree's maximum depth and leaf node. Also, the mean decrease in the impurity (MDI) of the RF impurity is employed to determine the aquifers that contribute the most to the subsidence in the study area. In the MDI, a variable with a significant reduction is considered essential in the impurity, and the more significant the mean decrease in impurity, the more influential the variable is (Tesoriero et al. 2017).

Also, KNN is an algorithm usually employed for classification analysis and is used in this study to understand the correlation between groundwater piezometric level and land deformation. It is mainly known as a nonparametric learning algorithm that does not consider any assumption in the data distribution. The model necessitates the selection of k, meaning the number of neighbors. The parameter 'k' in KNN is complex to identify and refers to the number of nearest neighbors comprising most of the voting process. It directs the voting system in the KNN, in

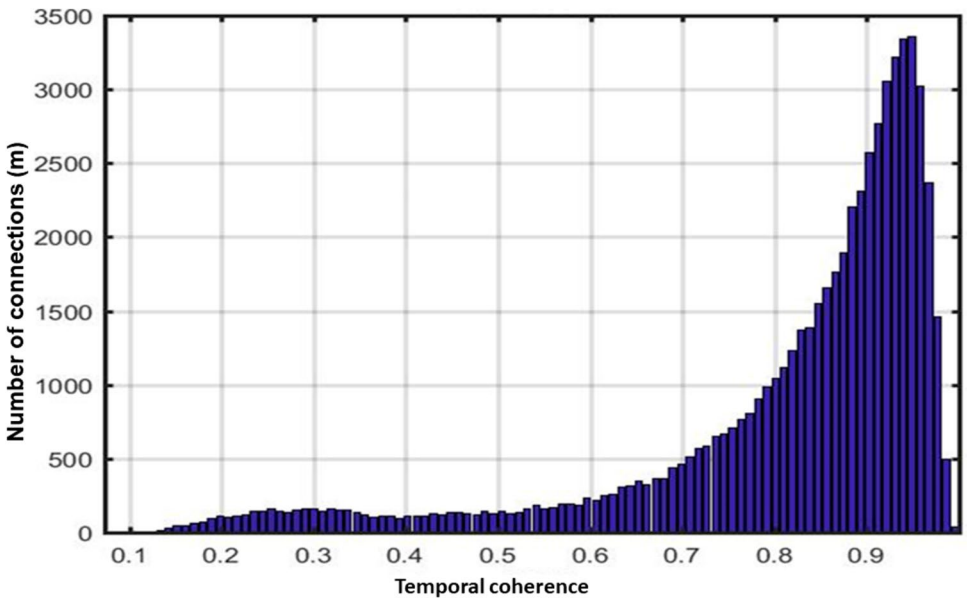

Fig. 4 Histogram showing the relationship between the number of connections and temporal coherence, evaluated to determine the atmospheric phase screen (APS)

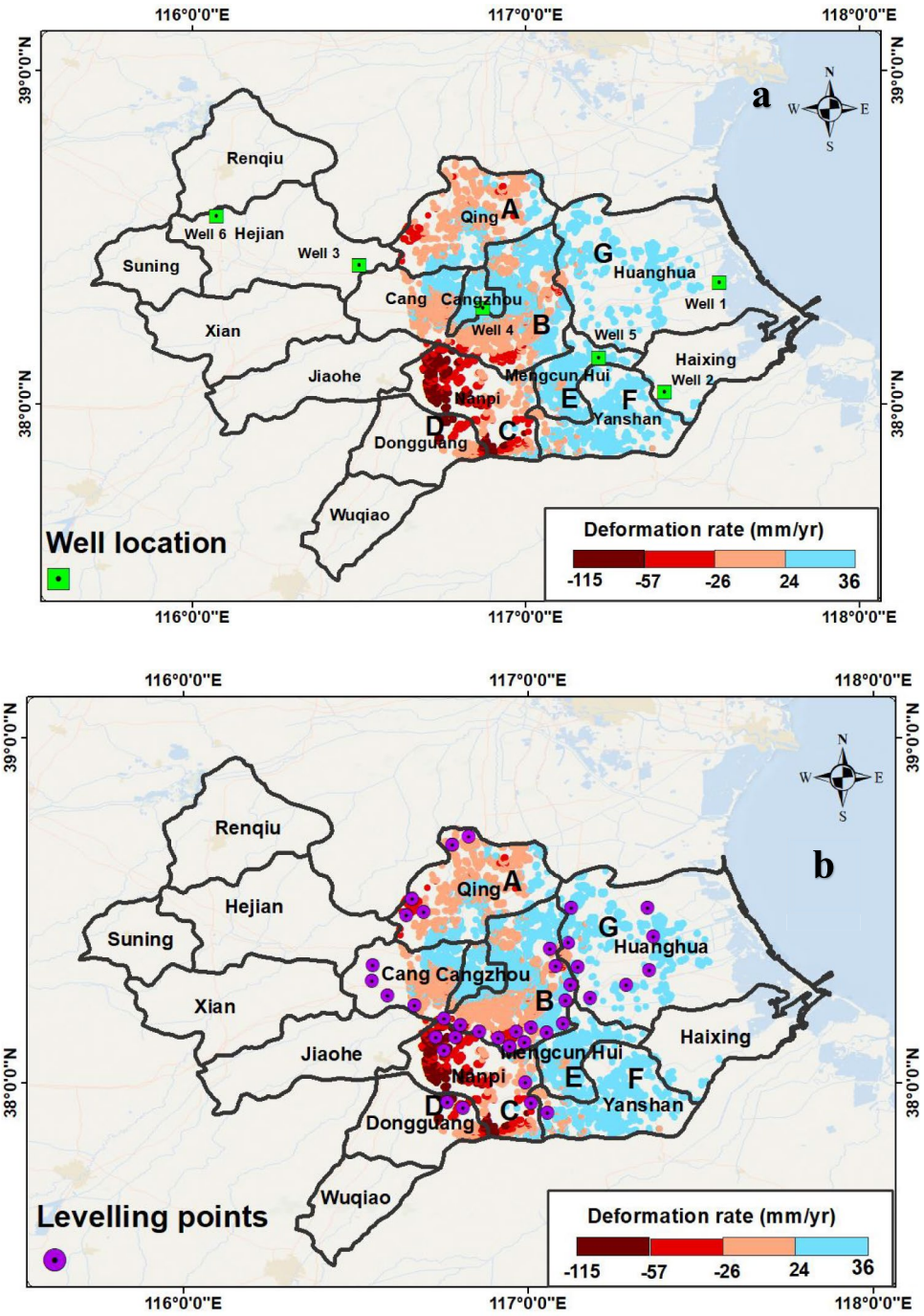

Fig. 5 Spatial distribution of land deformation rate using **a** the PS-InSAR technique and **b** the locations of the leveling points (Su et al. 2021)

which neighbors with the smallest distance are selected (Pham et al. 2021). In this analysis, the neighbor's value with the majority of voting is k, equal to 5. Therefore, to identify the number of the best neighbors for the model, the cross-validation data were selected from the training data to assess various k values. This process permits the label's prediction for every instance in the validation set using k (equal to 1, equal to 2, equal to 3….). It selects the value of k that gives the best performance on the validation set and uses that value in the final prediction for the algorithm. Therefore, the algorithm requires the k value and the distance function, and the model calculation distance is defined as the following Eq. (7):

$$\mathbf{K}(\mathbf{x}^*, \mathbf{y}) = \sqrt{\sum_{i=1}^{p} (\mathbf{x}^* - \mathbf{y})^2} \tag{7}$$

where $\mathbf{K}$ is the vector distance metric between two points, $\mathbf{y}$ is the parameter vector distance of the new dataset point,

which means the predicted values, $\mathbf{x}^*$ is the parameter vector of a single training data point in the independent variables, and p is the number of parameters used for prediction.

Model evaluation

The model's evaluation was done using a confusion matrix to measure the model's performance. A confusion matrix is a statistical metric to evaluate the performance of classification analysis (Nafouanti et al. 2023). This metric shows the capability of the model to forecast the actual compared to the predictive values. Therefore, sensitivity, specificity, accuracy, and error rate were computed from the confusion matrix. The different metrics equations are described by Eqs. (8)–(11) as follows (Fan et al. 2022):

$$\text{Sensitivity} = \frac{\text{TP}}{\text{TP} + \text{FN}} \tag{8}$$

$$\text{Specificity} = \frac{\text{TP}}{\text{TN} + \text{FP}} \tag{9}$$

$$\text{Errorrate} = \frac{\text{FP} + \text{FN}}{\text{TP} + \text{TN} + \text{FN} + \text{FP}} \tag{10}$$

$$\text{Acuracy} = \frac{\text{TP} + \text{TN}}{\text{TP} + \text{TN} + \text{FN} + \text{FP}} \tag{11}$$

where TP means true positives, which are instances where the model correctly identifies positive cases. The TN values are instances where the model correctly identifies negative cases. FP is the false positive, meaning the number of points predicted as having deformation while having no deformation. The false negative (FN) is the number of points predicted as having no subsidence while they do have subsidence.

Results and Discussion

Spatio-Temporal Subsidence Distribution in Cangzhou

PS-InSAR was employed to study the spatial distribution of land subsidence in Cangzhou using data from 2018 to 2022 after the South-to-North Water Diversion Project was initiated. As is well known, several studies have reported that severe subsidence caused by groundwater extraction was identified in the centre of Cangzhou (Gong et al. 2018; Su et al. 2021). The South-to-North Water Diversion Project started to supply water in Cangzhou in 2017 to alleviate the high subsidence in the area. Therefore, this research investigates the spatial distribution of the mean land deformation in the centre of Cangzhou from 2018 to 2022 (Fig. 5a). The region is divided into seven areas based on the counties that have subsidence above –20 mm/year and revealed that the mean deformation in the centre of Cangzhou varied between –115 to –26 mm/year obtained from the PS-InSAR technique. The most severe deformation was observed in areas C and D, with a maximum rate of –115 mm/year in Nanpi and east of Dogguang. In areas A and B, the deformation varies between –57 and –26 mm/year in Qingxian and Cangxian. The PS-InSAR technique also identifies a few deformation points higher than –20 mm/year in areas E, F, and G; however, several points in these areas (E, F, G) have no deformation. The safe areas with no deformation are shown as positive values in blue color (Fig. 5a). The results are consistent with previous studies that found a high deformation in the same counties, demonstrating the accurate results of the PS-InSAR technique (L. Bai et al. 2022; X. Bai et al. 2022; Zhou et al. 2018, 2017). Ground uplift is observed in the centre of Cangzhou (areas with positive values), which should be attributed to the increase in groundwater piezometric pressures due to restricting groundwater exploitation. The Cangzhou uplift is historically evident in the deformation centre (L. Bai et al. 2022; X. Bai et al. 2022). Land deformation is most observed in urban areas, specifically in central Cangzhou, caused by the dense population and thus increased industrial and agricultural activities, leading to more groundwater extraction before the SNWDP (Guo et al. 2015; Zhou et al. 2018). Another possible reason is the construction of heavyweight buildings (Khan et al. 2022).

Furthermore, PS-InSAR was validated by verifying the PS points with leveling measurements; thus, leveling data from 1990 to 2010 (Su et al. 2021) of the NCP and 38 leveling points were acquired in Cangzhou. The results of the PS-InSAR and the leveling points show a high correlation, reaching 0.94 (Fig. 6), demonstrating that the two sets of points revealed good reliability. The PS points and leveling have identified deformation areas of more than –20 mm/year, indicating severe deformation in those areas. Therefore, this confirms the PSI's consistency in quantifying land subsidence in urban areas. The locations of the leveling points are shown in Fig. 5b, and most are observed in areas B, D, C, and A. These results demonstrate that the PS-InSAR and the leveling are consistent in areas A, B, C, and D; however, the PS-InSAR identified several locations in area G as having no deformation, but this area is identified with more leveling points, which suggests that the deformation in that area is already recovered. The areas with high deformation with the PS-InSAR and the leveling approaches—such as Nanpi, Qinxian, Dongguang, and Cangxian—were also detected with high deformation in previous research (L. Bai et al. 2022; X. Bai et al. 2022; Zhou et al. 2018).

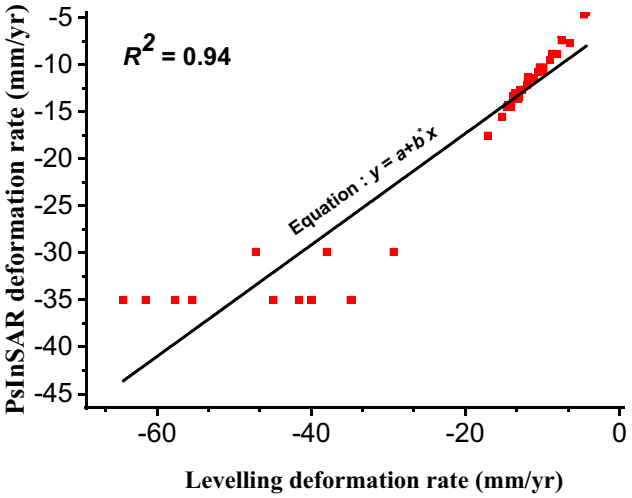

Fig. 6 Evaluation of land deformation rates obtained from the PS-InSAR and leveling measurements (Su et al. 2021)

Groundwater piezometric trends

Cangzhou has experienced extensive land deformation caused by groundwater extraction in confined aquifers, and the changes in piezometric pressure concur with the land deformation (L. Bai et al. 2022; X. Bai et al. 2022; Chen et al. 2020; Fan et al. 2021). Establishing the SNWDP project has reduced groundwater pumping compared with previous years (Hwang et al. 2016; Wang et al. 2019). The water level elevation from six wells in Fig. 7 demonstrates that in wells 1, 2, and 5, the water level was higher from 2017 to 2019, whereas from 2020 to 2022, the water level declined. The water level decline might be attributed to long-term groundwater extraction and less precipitation. In wells 3 and 6, in 2017, 2021, and 2022, the water levels were lower than from 2018 to 2020; additionally, well 4 shows a high-water level in 2017, 2018, and 2021 compared with 2019, 2020 and 2022. Therefore, it can be seen that after the SNDWP was initiated, the water level started to recover, but that a decrease has been observed in recent years, particularly in 2022, in the six wells. The reduction of groundwater level in recent years explains the presence of land deformation identified in the study area. Reduction of groundwater level in the wells can be caused by climate change, and by long-term droughts, which were also the principal reasons for the groundwater decline in Cangzhou (L. Bai et al. 2022; X. Bai et al. 2022). The drought climate has a double effect on groundwater variation. It decreases groundwater recharge, and more groundwater is extracted to provide the necessary water during droughts. Consequently, drought conditions will decrease the groundwater level, and land subsidence will intensify accordingly.

Furthermore, the groundwater level of aquifers I, II, III, and IV in July 2022 was observed at different locations within the study areas (Fig. 8). With GIS spatial analysis, the results show that in Nanpi, where the highest deformation rate reaches –115 mm/year, the groundwater level has been lowered by more than 78 m. In Cangxian and Qingxian, the groundwater level is lowered between 52 and 65 m, and those areas have moderate deformation, reaching –26 to –57 mm/year. The piezometric level in the confined aquifers in several counties of the study area has shown a significant decrease, which explains the current deformation observed in the area; therefore, groundwater restriction should be enhanced in the study area to recover the groundwater level to control land deformation.

Relationship between groundwater and land deformation using RF and KNN

The performance of RF and KNN using the confusion matrix was employed to understand the relationship between groundwater pressure and land subsidence in Cangzhou. The two models yielded satisfactory results in predicting land subsidence. The RF achieved an accuracy of 85%, sensitivity of 98%, specificity of 75%, and an error rate of 15% (Fig. 9). The model has shown a good performance due to its ability to identify high sensitivity. The high sensitivity predicted by the model confirmed the deformation rate identified in the study area, and the specificity demonstrates the areas with no deformation rate predicted by the model. Therefore, the RF's considerable accuracy, sensitivity, specificity, and lower error rate confirmed the random forest method's ability to predict land subsidence using groundwater pressure data. These results demonstrate that the water pressure change affects land deformation in the research area. The RF was previously employed to understand the relationship between groundwater pressure and land subsidence in Beijing, and the model demonstrated a high performance (Chen et al. 2020).

The results of the KNN revealed an accuracy, sensitivity, specificity, and error rate of 77, 89, 67, and 23%, respectively (Fig. 9). The KNN model demonstrates exemplary performance in forecasting land deformation using the groundwater level of the four aquifers. The model performs with high sensitivity and specificity, which suggests a high performance in terms of prediction; thus, the RF and KNN findings confirmed the consistent relationship between groundwater pressure and land deformation, constituting the leading cause of ground displacement in the research zone. The findings are consistent with previous studies, which revealed that groundwater extraction is the leading cause of land displacement in Cangzhou (L. Bai et al. 2022; X. Bai et al. 2022; Su et al. 2021; Sun et al. 2022).

The mean decrease in impurity has been employed to identify the aquifers that contribute the most to land deformation in the study area. The mean decrease in impurity is a measure of feature importance developed in RF. The features

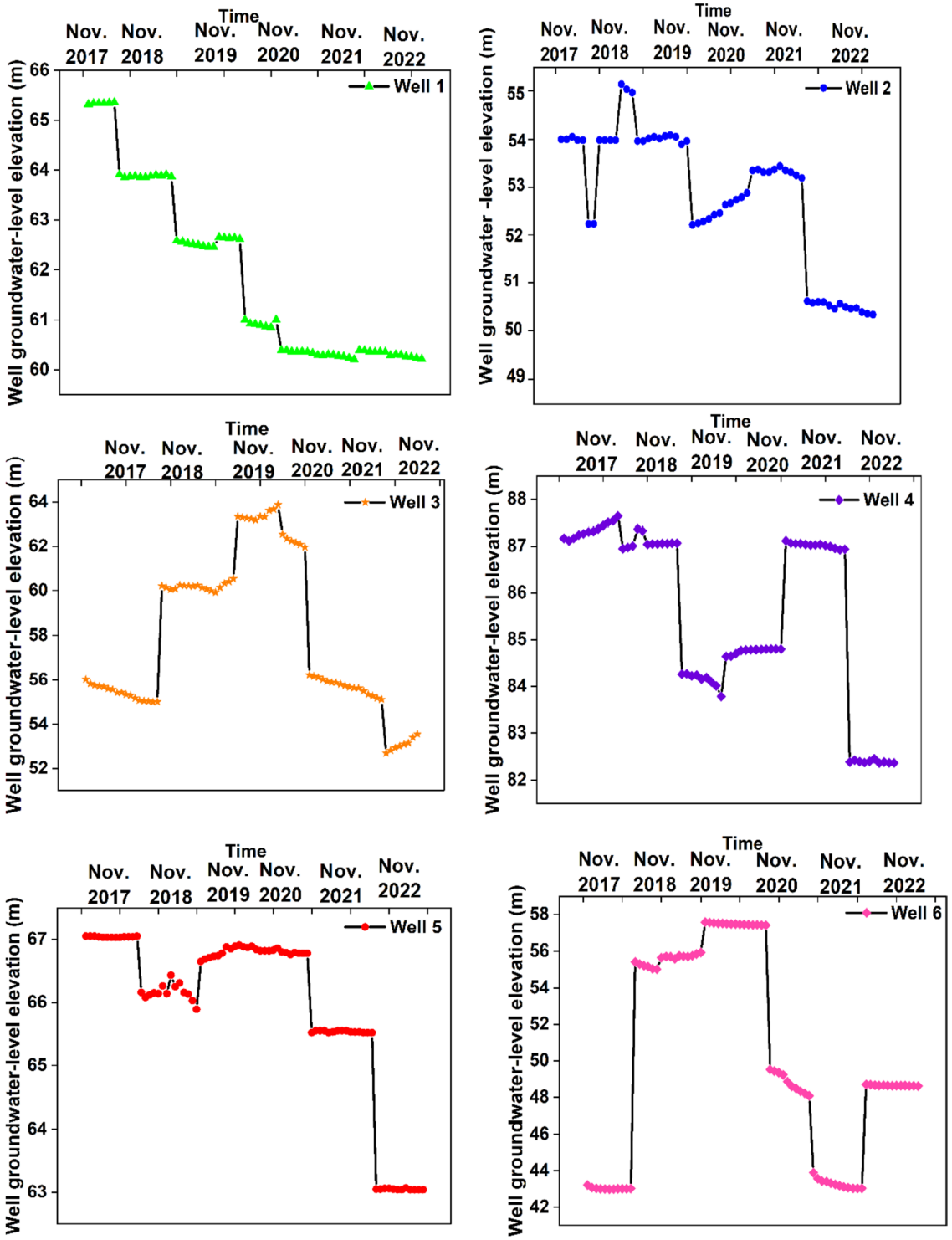

Fig. 7 Annual temporal variation of the groundwater-level elevation (m above sea level) in six wells in Cangzhou from 2017–2022 collected from different depths: well 1 at 291 m, well 2 at 329 m, well 3 at 343 m, well 4 at 346 m, well 5 at 472 m, and well 6 at 454 m bgl

that will split near the tree root have a high value (Calle and Urrea 2011; Wang et al. 2020); therefore, the important feature contributing to the output will be the largest in the plot with a significant mean decrease in impurity values (Fig. 10). Thus, aquifers IV and III have the highest values in the plot and have a mean decrease in the impurity of 33 and 26%, respectively, thus wielding the most influence on land deformation in the study area. Aquifers II and I have shown

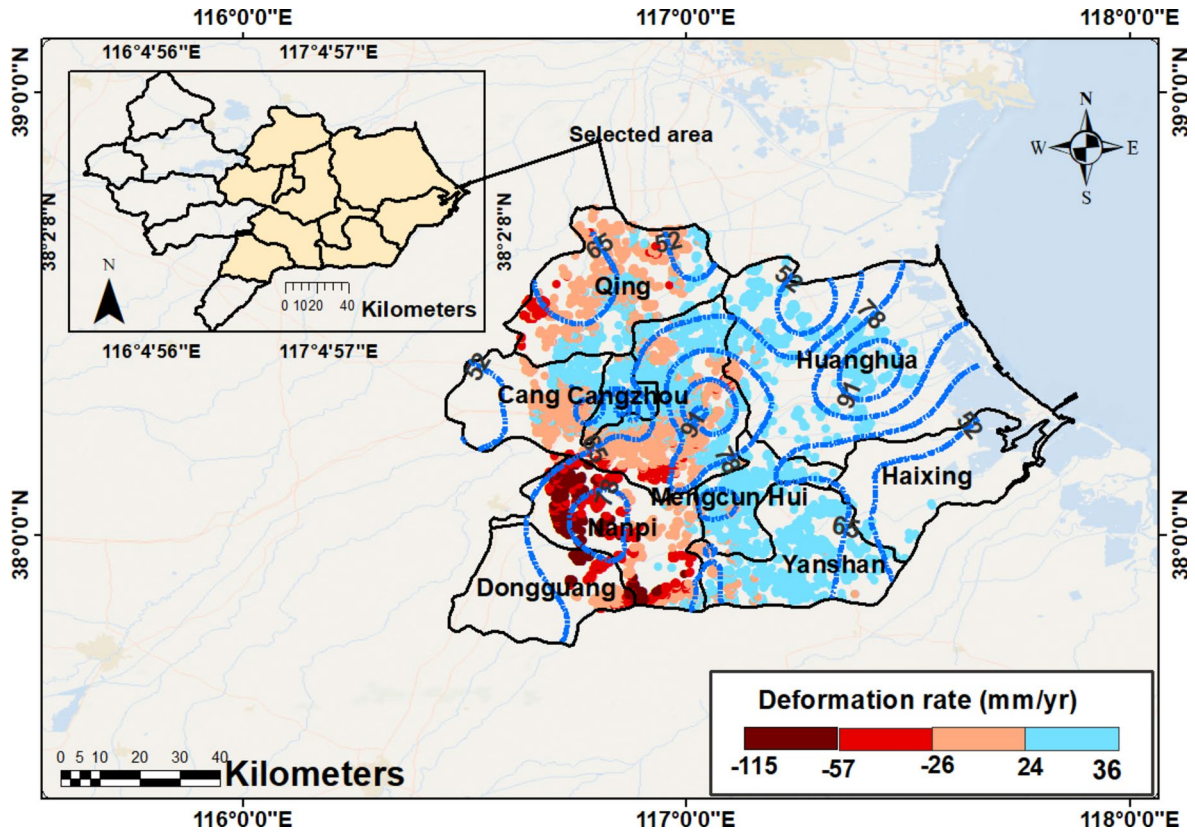

Fig. 8 Contours (m) of groundwater-level change in different wells obtained in July 2022

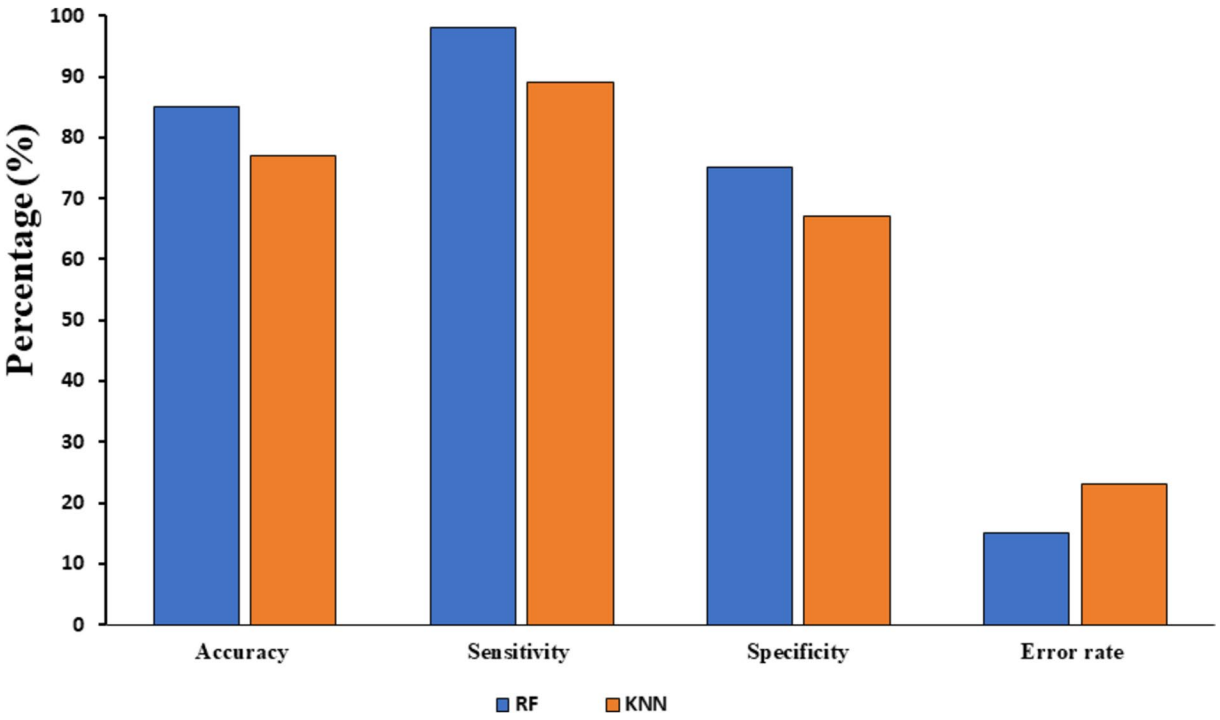

Fig. 9 Model performance using different evaluation metrics

a mean decrease in impurity of 24 and 20%, respectively. These results revealed that the decrease of groundwater pressure in the deep confined aquifers (III and IV) contributed the most to the land deformation in the study areas. These findings are consistent with previous works reporting that the main groundwater used in Cangzhou is from confined aquifers (L. Bai et al. 2022; X. Bai et al. 2022; Su et al. 2021; Wang et al. 2009). The water in the upper aquifer layers in Cangzhou is known to be brackish and saline (L. Bai et al. 2022; X. Bai et al. 2022); therefore, the groundwater is usually extracted from the confined aquifers III and IV, which explains the high influence of the confined aquifers on land subsidence in the study area. Also, the ability of the mean decrease in impurity to determine the input variables that contribute to output was reported in previous works (Bhattacharya and Mishra 2018; Dhiman and Keshari 2006).

Furthermore, the correlation between land subsidence and the water pressure of the confined aquifers (I, II, III, and IV) was investigated (Fig. 11), and the results reveal a correlation of 0.99, a result that demonstrates that land deformation and groundwater pressure have a consistent relationship. These results confirmed the finding of ML to identify the relationship between groundwater pressure and land deformation.

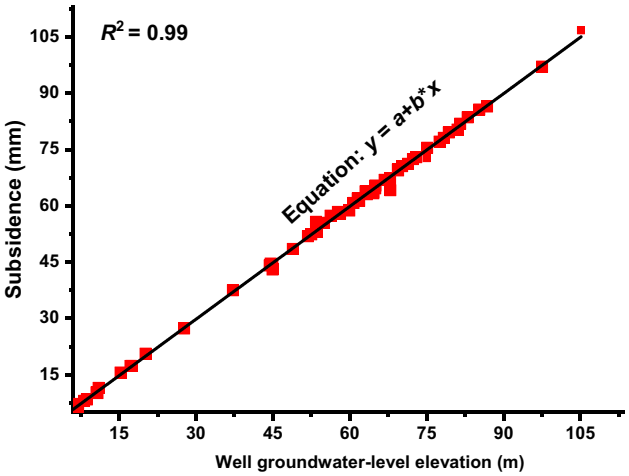

Fig. 11 Correlation between groundwater level in wells of the four aquifers (I, II, III, IV) and land subsidence

Effects of natural and human activities in Cangzhou

Human activities and natural factors contribute to land deformation on global and regional scales (Milillo et al. 2018). Cangzhou is an area of water scarcity caused by population growth and environmental pressure; thus, the lack of surface water and the high salinity in the shallow groundwater have led to overabstraction of the deep groundwater to maintain economic development and growth. The groundwater is principally abstracted for agriculture (about 66.1%) and drinking (Guo et al. 2015), whereas another factor is mining, which is often associated with subsidence in several parts of the world (Al Mukaimi et al. 2018). With the intensification of machine-operated wells for groundwater extraction and the increased mining activities, the groundwater level has dropped, and a regional groundwater depression cone has gradually formed in the NCP (Guo et al. 2015). Mining operations involve the extraction of valuable minerals or other geological materials from the earth. The water extracted from wells may serve several purposes in mining, such as cooling

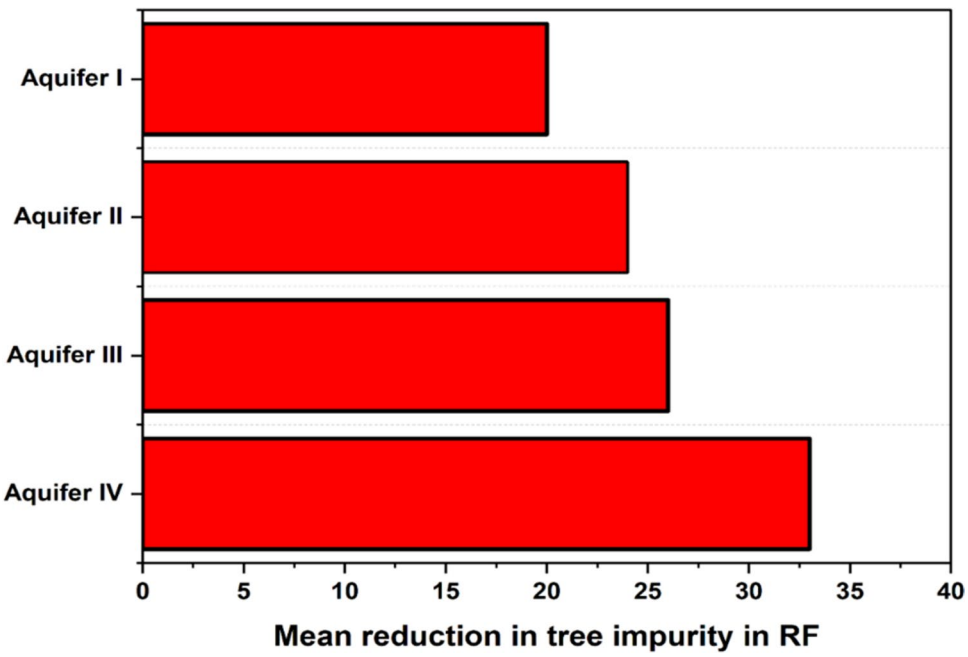

Fig. 10 Significant predictors to the subsidence using the mean decrease in impurity

and ore processing. With increased extraction, the pore-water pressure is reduced, and the clayey soil layers lose water due to compaction, resulting in land deformation. During 1996, the mean volume of mining material extracted in the region was 6.5×10^8 m^3. The volume in 2001–2003 was 9.2×10^8 m^3, which enhanced groundwater consumption (Shao et al. 2017). Likewise, silts and clays with organic matter in confined aquifers show high storativity and compressibility with low transmissivity, which influence land subsidence and have been revealed as a primary source of land deformation around the globe (Holzer and Johnson 1985).

Conclusion

The present research employed PS-InSAR to quantify the current land deformation situation in Cangzhou after implementing the South-to-North Water Diversion Project. Machine learning models, such as random forest (RF) and k-nearest neighbor (KNN), were also used to determine the relationship between groundwater pressure and land deformation. The findings demonstrated that the deformation rate in the area reached –115 mm/year, while several locations have deformation rates between –57 and –26 mm/year. Moreover, the results from the RF and KNN showed that the models suggested satisfactory results, with an accuracy, sensitivity, specificity, and error rate of 0.85, 98, 75, and 0.15% for the RF, and 77, 89, 67, and 0.23% for the KNN, respectively. Also, the value of the mean decrease in impurity was employed to find the aquifers that most influence land subsidence in the study area. The results showed that aquifers IV and III influenced the output most, followed by aquifers II and I; thus, the adopted techniques performed well in quantifying land subsidence and its relationship with groundwater pressure. These results revealed that PS-InSAR is a reliable technique for studying deformation in the area and can be implemented in many urban areas to quantify land subsidence. Machine learning models such as RF and KNN are suitable techniques to determine the relationship between groundwater pressure and land deformation, and they can be applied in other areas facing similar challenges. Therefore, future study needs to focus on developing powerful techniques to characterize each parameter responsible for land deformation and identify locations and livelihoods that may be affected by land deformation to improve sustainability.

Supplementary Information The online version contains supplementary material available at https://doi.org/10.1007/s10040-024-02771-5.

Acknowledgements The authors are grateful to all the researchers who contributed to the data collection and work undertaken as part of this research project, and for the support of the Chinese Government Scholarship (CSC). Also, we are grateful for the support from Jonathan Larkin and the *Hydrogeology Journal*'s technical editor Sue Duncan.

Funding The research work was financially supported by the National Natural Science Foundation of China (42,020,104,005 and 42,177,067), the Ministry of Education of China (111 project), and the Fundamental Research Funds for the Central Universities, China University of Geosciences (Wuhan).

Declarations

Conflict of interests The authors declare that they have no known competing financial interests or personal relationships that could have appeared to influence the work reported in this paper.

References

Abdollahi S, Pourghasemi HR, Ghanbarian GA, Safaeian R (2019) Prioritization of effective factors in the occurrence of land subsidence and its susceptibility mapping using an SVM model and their different kernel functions. Bull Eng Geol Environ 78:4017–4034. https://doi.org/10.1007/s10064-018-1403-6

Al Mukaimi ME, Dellapenna TM, Williams JR (2018) Enhanced land subsidence in Galveston Bay, Texas: interaction between sediment accumulation rates and relative sea level rise. Estuar Coast Shelf Sci 207:183–193

Arabameri A, Chandra Pal S, Rezaie F, Chakrabortty R, Chowdhuri I, Blaschke T, Thi Ngo PT (2021a) Comparison of multi-criteria and artificial intelligence models for land-subsidence susceptibility zonation. J Environ Manage 284:112067. https://doi.org/10.1016/j.jenvman.2021.112067

Arabameri A, Santosh M, Rezaie F, Saha S, Coastache R, Roy J, Mukherjee K, Tiefenbacher J, moayedi H (2021b) Application of novel ensemble models and k-fold CV approaches for Land subsidence susceptibility modelling. Stoch Environ Res Risk Assess 7. https://doi.org/10.1007/s00477-021-02036-7

Arangio S, Calò F, Di Mauro M, Bonano M, Marsella M, Manunta M (2014) An application of the SBAS-DInSAR technique for the assessment of structural damage in the city of Rome. Struct Infrastruct Eng 10:1469–1483

Argus DF, Heflin MB, Peltzer G, Crampé F, Webb FH (2005) Interseismic strain accumulation and anthropogenic motion in metropolitan Los Angeles. J Geophys Res Solid Earth 110(B4). https://doi.org/10.1029/2003JB002934

ASF DAAC (2015) Copernicus Sentinel data. Processed by ESA

Bai L, Jiang L, Zhao Y, Li Z, Cao G, Zhao C, Liu R, Wang H (2022) Quantifying the influence of long-term overexploitation on deep groundwater resources across Cangzhou in the North China Plain using InSAR measurements. J Hydrol 605:127368. https://doi.org/10.1016/j.jhydrol.2021.127368

Bai X, Li W, Lin X, Han L, Ming D (2022) Reconciling regional water diversion and urban growth policies to protect groundwater across a large urban region in China. J Hydrol 612:128094. https://doi.org/10.1016/j.jhydrol.2022.128094

Beladam O, Balz T, Mohamadi B, Abdalhak M (2019) Using PS-InSAR with Sentinel-1 images for deformation monitoring in northeast Algeria. Geosciences 9:315

Bhattacharya S, Mishra S (2018) Applications of machine learning for facies and fracture prediction using Bayesian Network Theory and Random Forest: case studies from the Appalachian basin. USA J Pet Sci Eng 170:1005–1017. https://doi.org/10.1016/j.petrol.2018.06.075

Borghero C (2018) Feasibility study of dam deformation monitoring in Northern Sweden using Sentinel1 SAR interferometry. Thesis, Univ. of Gävle, Sweden. https://www.diva-portal.org/smash/get/diva2:1173742/FULLTEXT01.pdf. Accessed January 2024

Budhu M, Adiyaman I (2013) The influence of clay zones on land subsidence from groundwater pumping. Groundwater 51:51–57
Bürgmann R, Rosen PA, Fielding EJ (2000) Synthetic aperture radar interferometry to measure Earth's surface topography and its deformation. Annu Rev Earth Planet Sci 28:169–209
Calle ML, Urrea V (2011) Letter to the editor: stability of random forest importance measures. Brief Bioinform 12:86–89. https://doi.org/10.1093/bib/bbq011
Chen B, Gong H, Chen Y, Li X, Zhou C, Lei K, Zhu L, Duan L, Zhao X (2020) Land subsidence and its relation with groundwater aquifers in Beijing Plain of China. Sci Total Environ 735:139111
Cian F, Blasco JMD, Carrera L (2019) Sentinel-1 for monitoring land subsidence of coastal cities in Africa using PSInSAR: a methodology based on the integration of SNAP and staMPS. Geosciences 9:124
Cigna F, Tapete D (2021) Sentinel-1 big data processing with P-SBAS InSAR in the geohazards exploitation platform: an experiment on coastal land subsidence and landslides in Italy. Remote Sens 13:885
Colesanti C, Ferretti A, Prati C, Rocca F (2003) Monitoring landslides and tectonic motions with the Permanent Scatterers Technique. Eng Geol 68:3–14
Da Lio C, Teatini P, Strozzi T, Tosi L (2018) Understanding land subsidence in salt marshes of the Venice Lagoon from SAR Interferometry and ground-based investigations. Remote Sens Environ 205:56–70
Dehghani M, Zoej MJV, Hooper A, Hanssen RF, Entezam I, Saatchi S (2013) Hybrid conventional and persistent scatterer SAR interferometry for land subsidence monitoring in the Tehran Basin. Iran ISPRS J Photogramm Remote Sens 79:157–170
Dhiman SD, Keshari AK (2006) Hydrogeochemical evaluation of high-fluoride groundwaters: a case study from Mehsana District, Gujarat. India Hydrol Sci J 51:1149–1162
Fan C, Song C, Liu K, Ke L, Xue B, Chen T, Fu C, Cheng J (2021) Century-Scale Reconstruction of Water Storage Changes of the Largest Lake in the Inner Mongolia Plateau Using a Machine Learning Approach. Water Resour Res 57. https://doi.org/10.1029/2020WR028831
Fan X, Wang X, Zhang X, Xiong ASCE (Bill) Yu PEF (2022) Machine learning based water pipe failure prediction: the effects of engineering, geology, climate, and socio-economic factors. Reliab Eng Syst Saf 219:108185. https://doi.org/10.1016/j.ress.2021.108185
Feng X, Chen Z, Li G, Ju Q, Yang Z, Cheng X (2023) Improving the capability of D-InSAR combined with offset-tracking for monitoring glacier velocity. Remote Sens Environ 285:113394
Figueroa-Miranda S, Tuxpan-Vargas J, Ramos-Leal JA, Hernández-Madrigal VM, Villaseñor-Reyes CI (2018) Land subsidence by groundwater over-exploitation from aquifers in tectonic valleys of Central Mexico: a review. Eng Geol 246:91–106. https://doi.org/10.1016/j.enggeo.2018.09.023
Gahalaut VK (2009) Coulomb stress change due to the 2005 Kashmir earthquake and implications for future seismic hazards. J Seismol 13:379–386
Gong H, Pan Y, Zheng L, Li X, Zhu L, Zhang C, Huang Z, Li Z, Wang H, Zhou C (2018) Long-term groundwater storage changes and land subsidence development in the North China Plain (1971–2015). Hydrogeol J 26:1417–1427. https://doi.org/10.1007/s10040-018-1768-4
Govil H, Tripathi MK, Guha S (2019) Deformation monitoring using D-InSAR technique in coalfield of Korba Chhattisgarh, India. In: 2019 16th International Conference on Electrical Engineering/Electronics, Computer, Telecommunications and Information Technology (ECTI-CON). IEEE, Piscataway, NJ, pp 681–684
Guo H, Zhang Z, Cheng G, Li W, Li T, Jiao JJ (2015) Groundwater-derived land subsidence in the North China Plain. Environ Earth Sci 74:1415–1427. https://doi.org/10.1007/s12665-015-4131-2
Guo H, Hao A, Li W, Zang X, Wang Y, Zhu J, Wang L, Chen Y (2022) Land subsidence and its affecting factors in Cangzhou, North China Plain. Front Environ Sci 10:1–17. https://doi.org/10.3389/fenvs.2022.1053362
Guzy A, Malinowska AA (2020) State of the art and recent advancements in the modelling of land subsidence induced by groundwater withdrawal. Water (Switzerland) 12. https://doi.org/10.3390/w12072051.
Hilley GE, Burgmann R, Ferretti A, Novali F, Rocca F (2004) Dynamics of slow-moving landslides from permanent scatterer analysis. Science 304 (80):1952–1955
Holzer TL, Galloway DL (2005) Impacts of land subsidence caused by the withdrawal of underground fluids in the United States. USGS. https://doi.org/10.1130/2005.4016(08)
Holzer TL, Johnson AI (1985) Land subsidence caused by ground water withdrawal in urban areas. GeoJ 11:245–255
Hooper A, Bekaert D, Spaans K, Arikan M (2012) Recent advances in SAR interferometry time series analysis for measuring crustal deformation. Tectonophysics 514–517:1–13. https://doi.org/10.1016/j.tecto.2011.10.013
Hussain MA, Chen Z, Shoaib M, Shah SU, Khan J, Ying Z (2022a) Sentinel-1A for monitoring land subsidence of coastal city of Pakistan using Persistent Scatterers In-SAR technique. Sci Rep 12:1–18. https://doi.org/10.1038/s41598-022-09359-7
Hussain MA, Chen Z, Zheng Y, Shoaib M, Shah SU, Ali N, Afzal Z (2022b) Landslide Susceptibility Mapping Using Machine Learning Algorithm Validated by Persistent Scatterer In-SAR Technique. Sensors 22. https://doi.org/10.3390/s22093119
Hwang C, Yang Y, Kao R, Han J, Shum CK, Galloway DL, Sneed M, Hung W-C, Cheng Y-S, Li F (2016) Time-varying land subsidence detected by radar altimetry: California, Taiwan, and north China. Sci Rep 6:1–12
Jordan MI, Mitchell TM (2015) Machine learning: trends, perspectives, and prospects. Science 349(80):255–260
Kaneda H, Nakata T, Tsutsumi H, Kondo H, Sugito N, Awata Y, Akhtar SS, Majid A, Khattak W, Awan AA (2008) Surface rupture of the 2005 Kashmir, Pakistan, earthquake and its active tectonic implications. Bull Seismol Soc Am 98:521–557
Khan J, Ren X, Hussain MA, Jan MQ (2022) Monitoring land subsidence using PS-InSAR technique in Rawalpindi and Islamabad, Pakistan. Remote Sens 14. https://doi.org/10.3390/rs14153722
Khorrami M, Abrishami S, Maghsoudi Y, Alizadeh B, Perissin D (2020) Extreme subsidence in a populated city (Mashhad) detected by PSInSAR considering groundwater withdrawal and geotechnical properties. Sci Rep 10:11357
Lei KC, Luo Y, Chen BB, Guo G, Zhou Y (2016) Distribution characteristics and influence factors of land subsidence in Beijing area. Geol China 43:2216–2225
Li X, Li G, Zhang Y (2014) Identifying major factors affecting groundwater change in the North China Plain with grey relational analysis. Water 6:1581–1600
Mateos RM, Ezquerro P, Luque-Espinar JA, Béjar-Pizarro M, Notti D, Azañón JM, Montserrat O, Herrera G, Fernández-Chacón F, Peinado T (2017) Multiband PSInSAR and long-period land subsidence monitoring in a strategic detrital aquifer (Vega de Granada, SE Spain): an approach to support management decisions. J Hydrol 553:71–87
Milillo P, Giardina G, DeJong MJ, Perissin D, Milillo G (2018) Multi-temporal InSAR structural damage assessment: the London Crossrail case study. Remote Sens 10:287
Nafouanti MB, Li J, Nyakilla EE, Mwakipunda GC, Mulashani A (2023) A novel hybrid random forest linear model approach for forecasting groundwater fluoride contamination. Environ Sci Pollut Res 30:50661–50674
Ng AH-M, Ge L, Li X (2015) Assessments of land subsidence in the Gippsland Basin of Australia using ALOS PALSAR data. Remote Sens Environ 159:86–101

Ohenhen LO, Shirzaei M (2022) Land subsidence hazard and building collapse risk in the coastal city of Lagos, West Africa. Earth's Futur 10:e2022EF003219

Pang B, Fu F, Wang L (2014) Underground water mining restriction and physical mechanism analysis in Cangzhou. Water Technol 8:45–49

Pham BT, Nguyen MD, Nguyen-Thoi T, Ho LS, Koopialipoor M, Kim Quoc N, Armaghani DJ, Le HV (2021) A novel approach for classification of soils based on laboratory tests using Adaboost, Tree, and ANN modeling. Transp Geotech 27:100508. https://doi.org/10.1016/j.trgeo.2020.100508

Pinel V, Hooper A, De la Cruz-Reyna S, Reyes-Davila G, Doin MP, Bascou P (2011) The challenging retrieval of the displacement field from InSAR data for andesitic stratovolcanoes: case study of Popocatepetl and Colima Volcano, Mexico. J Volcanol Geotherm Res 200:49–61

Podgorski JE, Labhasetwar P, Saha D, Berg M (2018) Prediction modeling and mapping of groundwater fluoride contamination throughout India. Environ Sci Technol 52:9889–9898. https://doi.org/10.1021/acs.est.8b01679

Pourkhosravani M, Mehrabi A, Pirasteh S, Derakhshani R (2022) Monitored the Maskun landslide and determined its quantitative relationship to different climatic conditions using D-InSAR and PSI techniques. Geom Nat Hazards Risk 13:1134–1153

Prati C, Ferretti A, Perissin D (2010) Recent advances on surface ground deformation measurement by means of repeated space-borne SAR observations. J Geodyn 49:161–170

Rahmati O, Choubin B, Fathabadi A, Coulon F, Soltani E, Shahabi H, Mollaefar E, Tiefenbacher J, Cipullo S, Ahmad BB (2019a) Predicting uncertainty of machine learning models for modelling nitrate pollution of groundwater using quantile regression and UNEEC methods. Sci Total Environ 688:855–866

Rahmati O, Falah F, Naghibi SA, Biggs T, Soltani M, Deo RC, Cerdà A, Mohammadi F, Tien Bui D (2019b) Land subsidence modelling using tree-based machine learning algorithms. Sci Total Environ 672:239–252. https://doi.org/10.1016/j.scitotenv.2019.03.496

Ranjgar B, Razavi-Termeh SV, Foroughnia F, Sadeghi-Niaraki A, Perissin D (2021) Land subsidence susceptibility mapping using persistent scatterer SAR interferometry technique and optimized hybrid machine learning algorithms. Remote Sens 13. https://doi.org/10.3390/rs13071326

Rateb A, Abotalib AZ (2020) Inferencing the land subsidence in the Nile Delta using Sentinel-1 satellites and GPS between 2015 and 2019. Sci Total Environ 729:138868

Raz P, Sumantyo JTS, Widodo J, Izumi Y, Perissin D (2020) Land Deformation monitoring using the D-InSar technique during Lombok earthquake observed by Sentinel-1A/B. GEOMATE J 19:257–262

Ruiz-Armenteros AM, Lazecky M, Hlaváčová I, Bakoň M, Delgado JM, Sousa JJ, Lamas-Fernández F, Marchamalo M, Caro-Cuenca M, Papco J (2018) Deformation monitoring of dam infrastructures via spaceborne MT-InSAR: the case of La Viñuela (Málaga, southern Spain). Procedia Comput Sci 138:346–353

Schlögel R, Doubre C, Malet J-P, Masson F (2015) Landslide deformation monitoring with ALOS/PALSAR imagery: a D-InSAR geomorphological interpretation method. Geomorphology 231:314–330

Schmidt K, Schwerdt M, Ramon NT, Alfonzo GC, Döring B, Raab S, Reimann J, Rudolf D, Antony JW (2015) Verification of the Sentinel-1A SAR Instrument Calibration using active and passive Point Targets. In: Wave Propagation in Communication, Microwaves Systems and Navigation (WFMN) conference, Chemnitz, Germany, February 2015

Schneider RZ, Papathanassiou KP, Hajnsek I, Moreira A (2006) Polarimetric and interferometric characterization of coherent scatterers in urban areas. IEEE Trans Geosci Remote Sens 44:971–984

Shao W, Zhou J, Liu J, Zhang H, Wang J, Xiang C, Yang G, Tang Y (2017) An effect analysis of comprehensive treatment of groundwater over-exploitation in Cheng'an County, Hebei Province, China. Int J Environ Res Public Health 14:41

Shi M, Gong H, Gao M, Chen B, Zhang S, Zhou C (2020) Recent ground subsidence in the North China Plain, China, was revealed by Sentinel-1A datasets. Remote Sens 12:1–19. https://doi.org/10.3390/rs12213579

Sivasithamparam N, Karstunen M, Bonnier P (2015) Modelling creep behaviour of anisotropic soft soils. Comput Geotech 69:46–57. https://doi.org/10.1016/j.compgeo.2015.04.015

Su G, Wu Y, Zhan W, Zheng Z, Chang L, Wang J (2021) Spatiotemporal evolution characteristics of land subsidence caused by groundwater depletion in the North China plain during the past six decades. J Hydrol 600:126678. https://doi.org/10.1016/j.jhydrol.2021.126678

Suksathien Y, Chuvanichanon P, Tippimanchai T, Sueajui J (2022) Insufficient lateral stem contact is an influencing factor for significant subsidence in cementless short-stem total hip arthroplasty. World J Orthop 13:444–453. https://doi.org/10.5312/wjo.v13.i5.444

Sun D, Li J, Li H, Liu Q, Zhao S, Huang Y, Wu Q, Xie X (2022) Evolution of groundwater salinity and fluoride in the deep confined aquifers of Cangzhou in the North China plain after the South-to-North Water Diversion Project. Appl Geochem 147:105485. https://doi.org/10.1016/j.apgeochem.2022.105485

Tesoriero AJ, Gronberg JA, Juckem PF, Miller MP, Austin BP (2017) Predicting redox-sensitive contaminant concentrations in groundwater using random forest classification. Water Resour Res 53:7316–7331

Tovar-Gómez R, Moreno-Virgen MR, Dena-Aguilar JA, Hernández-Montoya V, Bonilla-Petriciolet A, Montes-Morán MA (2013) Modeling of fixed-bed adsorption of fluoride on bone char using a hybrid neural network approach. Chem Eng J 228:1098–1109. https://doi.org/10.1016/j.cej.2013.05.080

Vickers NJ (2017) Animal communication: when I'm calling you, will you answer too? Curr Biol 27:R713–R715

Wang K, Zhang R, Hiroshi Y (2009) Characterizing heterogeneous soil water flow and solute transport using information measures. J Hydrol 370:109–121

Wang S-J, Lee C-H, Hsu K-C (2015) A technique for quantifying groundwater pumping and land subsidence using a nonlinear stochastic poroelastic model. Environ Earth Sci 73:8111–8124

Wang S, Li J, Zhang B, Lee Z, Spyrakos E, Feng L, Liu C, Zhao H, Wu Y, Zhu L, Jia L, Wan W, Zhang F, Shen Q, Tyler AN, Zhang X (2020) Changes of water clarity in large lakes and reservoirs across China observed from long-term MODIS. Remote Sens Environ 247:111949. https://doi.org/10.1016/j.rse.2020.111949

Wang Y, Chen Y, Guo H, Zang X (2019) Study on compaction mechanism of overconsolidated soil and critical groundwater level in Cangzhou. In: E3S Web Conf, vol 79. https://doi.org/10.1051/e3sconf/20197902010

Xu YS, Shen SL, Ren DJ, Wu HN (2016) Analysis of factors in land subsidence in Shanghai: a view based on a strategic environmental assessment. Sustain 8. https://doi.org/10.3390/su8060573

Yang Q, Ke Y, Zhang D, Chen B, Gong H, Lv M, Zhu L, Li X (2018) Multi-scale analysis of the relationship between land subsidence and buildings: a case study in an eastern Beijing urban area using the PS-InSAR technique. Remote Sens 10:1006

Yao J, Yao X, Wu Z, Liu X (2021) Research on surface deformation of ordos coal mining area by integrating multitemporal D-InSAR and offset tracking technology. J Sensors 2021:1–14

Ye S, Xue Y, Wu J, Yan X, Yu J (2016) Progression and mitigation of land subsidence in China. Hydrogeol J 24:685–693

Zhang Z, Shi D, Ren F, Yin Z, Sun J, Zhang C (1997) Evolution of Quaternary groundwater system in North China Plain. Sci China Earth Sci 40:276

Zhao C, Lu Z, Zhang Q, de La Fuente J (2012) Large-area landslide detection and monitoring with ALOS/PALSAR imagery data over northern California and southern Oregon, USA. Remote Sens Environ 124:348–359

Zhao Q, Lin H, Jiang L, Chen F, Cheng S (2009) A study of ground deformation in the Guangzhou urban area with persistent scatterer interferometry. Sensors 9:503–518

Zhou C, Gong H, Chen B, Li X, Li J, Wang X, Gao M, Si Y, Guo L, Shi M, Duan G (2019) Quantifying the contribution of multiple factors to land subsidence in the Beijing Plain, China, with machine learning technology. Geomorphology 335:48–61. https://doi.org/10.1016/j.geomorph.2019.03.017

Zhou H, Wang Y, Yan S (2017) Study on land subsidence in Cangzhou area based on Sentinel-1A/B data. Int. Arch. Photogramm. Remote Sens. Spatial Inf. Sci. XLII-2/W7, pp 675–582. https://doi.org/10.5194/isprs-archives-XLII-2-W7-675-2017

Zhou H, Wang Y, Yan S, Li Y, Liu X, Zhang F (2018) Monitoring of recent ground surface subsidence in the Cangzhou region by the use of the InSAR time-series technique with multi-orbit Sentinel-1 TOPS imagery. Int J Remote Sens 39:8113–8128. https://doi.org/10.1080/01431161.2018.1482020

Zhou J, Her YG, Niu B, Zhao M, Li X, Yu X (2020) Regional-scale monitoring of underwater and dry ground subsidence in high phreatic areas of North China Plain. PLoS ONE 15:1–12. https://doi.org/10.1371/journal.pone.0237878

Zhu JY, Guo HP (2014) Relation between land subsidence and deep groundwater exploitation in Cangzhou City. Adv Mater Res 864–867:2213–2217. https://doi.org/10.4028/www.scientific.net/AMR.864-867.2213

Zuo J, Gong H, Chen B, Liu K, Zhou C, Ke Y (2019) Time-series evolution patterns of land subsidence in the Eastern Beijing Plain, China. Remote Sens 11:1–19. https://doi.org/10.3390/rs11050539